Numerical simulation of electrospray in the cone-jet mode

M. A. Herrada, J. M. López-Herrera, and A. M. Gañán-Calvo

Departamento de Ingeniería Aeroespacial y Mecánica de Fluidos, Universidad de Sevilla, E-41092 Sevilla, Spain

E. J. Vega and J. M. Montanero

Departamento de Ingeniería Mecánica, Energética y de los Materiales, Universidad de Extremadura, E-06006 Badajoz, Spain

S. Popinet

National Institute of Water and Atmospheric Research, P.O. Box 14-901, Kilbirnie, Wellington, New Zealand

We present a robust and computationally efficient numerical scheme for simulating steady electrohydrodynamic atomization processes (electrospray). The main simplification assumed in this scheme is that all the free electrical charges are distributed over the interface. A comparison of the results with those calculated with a volume-of-fluid method showed that the numerical scheme presented here accurately describes the flow pattern within the entire liquid domain. Experiments were performed to partially validate the numerical predictions. The simulations reproduced accurately the experimental shape of the liquid cone jet, providing correct values of the emitted electric current even for configurations very close to the cone-jet stability limit.

PACS number(s): 47.61.Jd, 47.65.−d, 47.55.−t, 47.15.−x

I. INTRODUCTION

The use of electrostatic fields to spray liquids is a procedure that has been used since the XVIIth century [1]. In the most typical configuration, the liquid is injected at a small flow rate through a metallic needle where an electric potential of the order of kilovolts is imposed with respect to a grounded electrode situated downstream. Although many electrospray modes have been identified [2], the one that has attracted the most attention is the cone-jet mode. In this mode, the meniscus adopts a stable quasiconical shape from whose apex a stationary thin jet is ejected. The jet eventually breaks up into droplets due to the capillary forces, which gives rise to a charged mist.

All theories describing the physics behind the cone-jet mode distinguish three regions [3,4]: (i) the upstream meniscus region attached to the needle, where ohmic conduction is the dominant mechanism of charge transport and the voltage drop is negligible; (ii) the downstream jet region, where the relevant charge transport mechanism is surface convection; and (iii) an intermediate transition region (the cone neck), where the charge transport mechanism evolves from conduction dominant to convection dominant. It is generally accepted that both the electric current circulating through the system and the jet's diameter are essentially governed by this neck region. Two theoretical approaches have been proposed to model this critical region: One considers electrical relaxation phenomena in this region [5] and the other assumes that the electric charges are relaxed over the entire interface, including the cone neck region [3,6,7]. They propose different scaling laws for both the jet's size and issued electric current. Experimental data for the size of the resulting droplets seem to indicate that the jet's diameter scales with the governing parameters as indicated by the later theory [8]. However, there have as yet been no experimental data on the neck clearly in favor of one or the other of these two approaches.

There have been several numerical studies of electrospray in the literature. The first numerical simulation was due to Hartman *et al.* [9], who used a one-dimensional model to reach steady cone-jet configurations by successive iterations. Their study focused on describing the meniscus and the neck regions. Yan *et al.* [10] refined that model by solving the axisymmetric Navier-Stokes equations and incorporating grid adaptation into their calculations. An additional constraint imposed in these two studies, even though it is not common operational practice, is that the jet is forced to hit a flat grounded electrode located downstream. Higuera [11] examined numerically the neck region in order to analyze the electric current circulating through the system. The presence of the needle and the breakup region were obviated by using as upstream and downstream boundary conditions far-field asymptotic behaviors for the conical meniscus [12,13] and the jet [3], respectively. In all these studies, the flow was assumed to be strictly steady, thus neglecting the growth of perturbations on the free surface and the subsequent jet breakup. Collins *et al.* [14] proposed a more sophisticated numerical scheme to study the entire electrohydrodynamic (EHD) tip streaming flow, including the formation of the cusp, the emitted jet, and the resulting droplets. Despite the disparity of the length scales present in this phenomenon, it was accurately described by this numerical approach. Reznik *et al.* [15] studied the temporal evolution of an electrified compound core-shell droplet towards the emission of a coaxial jet. All the aforementioned numerical studies have in common that, in the bulk, the electrical relaxation time was short compared to any hydrodynamic time present in the process and thus the liquid bulk was free of electrical charges, which were only allowed to exist at the interface. Consequently, the surface charge density σ_e was regarded as an unknown governed by the surface balance equation [5]

$$\frac{d(2\pi F u_s \sigma_e)}{ds} = 2\pi F K E^{\text{ni}}, \tag{1}$$

where s is the distance along the interface, F and u_s are the interface radial position and velocity, respectively, K is the
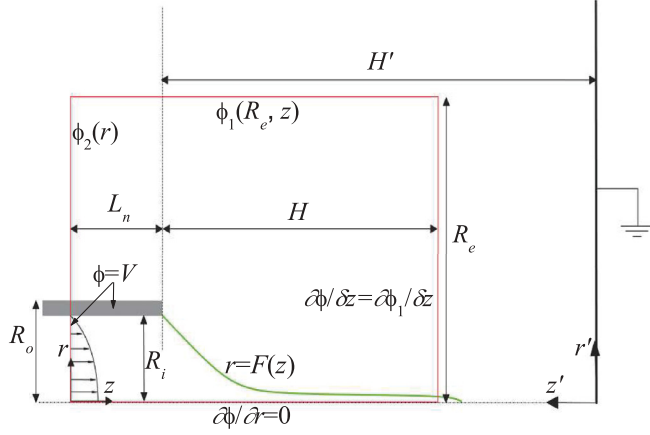
FIG. 1. (Color online) Sketch of the problem's formulation. The (red) rectangle denotes the limits of the computational domain.

liquid electrical conductivity, and E^{ni} is the normal component of the electric field on the inner side of the interface.

Besides the aforementioned works, numerical analyses of the cone jet mode can be found in the literature in which unconventional models for the electrical behaviors have been used. Lastow and Balachandran [16] assumed a dielectric behavior by neglecting the electric current, which seems to be a clear oversimplification since both experimental and theoretical works point to the relevance of the conductivity in the scaling of the emitted droplets. In the same line, Lim *et al.* [17] used a constant surface charge density over the entire cone-jet structure, adjusting its value by fitting numerical simulations to experiments. Both works showed a strong stretching of the meniscus by electrical means despite the feeble physical ground on which their electric models were built.

In the present work, a robust and computationally efficient numerical method is developed to simulate steady EHD atomization processes. As in previous approaches [9–11,14], the electric charges are confined to the interface. The results are compared with those calculated with GERRIS, an open source free software library developed by Popinet [18,19] and extended by López-Herrera *et al.* [20] to study EHD phenomena. Experiments are conducted to partially validate the numerical results. The cone-jet transition is examined very close to the stability limit to assess the validity of the hypothesis on the charge behavior.

The rest of the paper is organized as follows. The problem is formulated in Sec. II. Sections III and IV give the descriptions of the numerical schemes and the experimental method, respectively. Finally, the results are presented and discussed in Sec. V.

II. FORMULATION OF THE PROBLEM

The geometrical and electrical configurations considered in this work are represented schematically in Fig. 1. A metallic needle of inner radius R_i and outer radius R_o is held at a constant voltage V. The needle is brought face to face up close to a planar grounded electrode located at a distance H'. A liquid of density ρ, viscosity μ, electrical conductivity K, and permittivity ε is injected through the needle at a constant flow

rate Q. The flow is fully developed inside the capillary so that there is a parabolic Hagen-Poiseuille velocity profile upstream at a distance L_n from the needle's exit. The ambient medium is a perfect dielectric gas of permittivity ε_0 equal to that of the vacuum. The gas-liquid surface tension is γ. Because of the small values of the Bond number and gas-to-liquid density and viscosity ratios, the effects of gravity and the gas dynamics can be neglected.

The equations are made dimensionless with the inner radius R_i, the liquid density ρ, the surface tension γ, and the applied voltage V, which yields the characteristic time and velocity scales $t_c = (\rho R_i^3/\gamma)^{1/2}$ and $v_c = R_i/t_c$, respectively. The dimensionless axisymmetric incompressible Navier-Stokes equations for the liquid velocity $\mathbf{v}(r,z;t)$ and pressure $p(r,z;t)$ fields are

$$(ru)_r + rw_z = 0, \tag{2}$$

$$u_t + uu_r + wu_z = -p_r + C[u_{rr} + (u/r)_r + u_{zz}] + \chi f_e^r, \tag{3}$$

$$w_t + uw_r + ww_z = -p_z + C[w_{rr} + w_r/r + w_{zz}] + \chi f_e^z, \tag{4}$$

where t is the time, r (z) is the radial (axial) coordinate, u (w) is the radial (axial) velocity component, $\chi = \varepsilon_0 V^2/R_i\gamma$ is the electric Bond number, and $C = \mu(\rho\gamma R_i)^{-1/2}$ is the Ohnesorge number. The subscripts t, r, and z here and henceforth denote the partial derivatives with respect to the corresponding variables. The term f_e^r (f_e^z) stands for the radial (axial) volumetric electric force

$$\begin{pmatrix} f_e^r \\ f_e^z \end{pmatrix} = \rho_e \begin{pmatrix} E^r \\ E^z \end{pmatrix} - \frac{(E^r + E^z)^2}{2} \begin{pmatrix} \beta_r \\ \beta_z \end{pmatrix}, \tag{5}$$

where ρ_e is the volumetric charge density, E^r (E^z) is the radial (axial) electric field, and $\beta = \varepsilon/\varepsilon_0$ is the relative permittivity.

In addition to the Navier-Stokes equations for the liquid flow, the electric potentials ϕ^i and ϕ^o in both the inner (liquid) and outer (gas) domains must be calculated. They obey the Poisson and the Laplace equations

$$\phi_{zz}^i + \phi_{rr}^i + \phi_r^i/r = \rho_e/\beta, \tag{6}$$

$$\phi_{zz}^o + \phi_{rr}^o + \phi_r^o/r = 0, \tag{7}$$

respectively.

Taking into account the kinematic compatibility and equilibrium of tangential and normal stresses at the interface $r = F(z)$, one gets the following equations:

$$F_z w - u = 0, \tag{8}$$

$$C\frac{(1 - F_z^2)(w_r + u_z) + 2F_z(u_r - w_z)}{(1 + F_z^2)^{1/2}} = \chi\sigma_e E^t, \tag{9}$$

$$p + \frac{FF_{zz} - 1 - F_z^2}{F(1 + F_z^2)^{3/2}} - \frac{2C[u_r - F_z(w_r + u_z) + F_z^2 w_z]}{1 + F_z^2}$$
$$= \frac{\chi}{2}[(E^{\mathrm{no}})^2 - \beta(E^{\mathrm{ni}})^2 + (\beta - 1)(E^t)^2], \tag{10}$$

where σ_e is the surface charge density, E^t is the tangential component of the electric field, and E^{ni} and E^{no} are the normal components of the electrical field on the inner and outer sides of the interface, respectively. The right-hand sides of Eqs. (9) and (10) are the Maxwell stresses resulting from the accumulation of free electric charges at the interface and the jump of permittivity across this surface.

The electrical field and the surface charge density can be calculated from the inner ϕ^i and outer ϕ^o electric potentials and the free surface shape F:

$$E^{ni} = \frac{F_z \phi_z^i - \phi_r^i}{\sqrt{1 + F_z^2}}, \tag{11}$$

$$E^{no} = \frac{F_z \phi_z^o - \phi_r^o}{\sqrt{1 + F_z^2}}, \tag{12}$$

$$E^t = \frac{-F_z \phi_r^o + \phi_z^o}{\sqrt{1 + F_z^2}} = \frac{-F_z \phi_r^i + \phi_z^i}{\sqrt{1 + F_z^2}}, \tag{13}$$

$$\sigma_e = E^{no} - \beta E^{ni}. \tag{14}$$

Note that the continuity of the electric potential across the interface $\phi^i = \phi^o$ has been taken into account in Eq. (13). The interfacial equations are completed by imposing the surface charge conservation at the free surface $r = F(z)$ [Eq. (1)] [21]:

$$\frac{F_z u + w}{1 + F_z^2} \sigma_{ez} - \frac{\sigma_e}{1 + F_z^2} \left[u_r + F_z^2 w_z - F_z(u_z + w_r) \right] = \alpha E^{ni}, \tag{15}$$

where $\alpha = \beta(\rho R_i^3 K^2 / \gamma \varepsilon^2)^{1/2}$ is the dimensionless electrical conductivity.

We shall assume that all characteristic times of hydrodynamic nature are long compared to the electrical relaxation time (Saville's leaky dielectric model [22]). Therefore, the volumetric charge density ρ_e is zero and the liquid conductivity K is constant over the entire liquid domain. Also, the liquid electrical permittivity is assumed to be homogeneous and thus the volumetric dielectrophoretic force proportional to the permittivity gradient is zero. In this case, the electrical effects on the liquid dynamics are exclusively associated with the Maxwell stresses at the interface.

As mentioned above, a Hagen-Poiseuille velocity profile is assumed at the entrance of the liquid domain $z = 0$:

$$u = 0, \quad w = 2v_e(1 - r^2), \tag{16}$$

where $v_e = Q/\pi R_i^2 v_c$ is the dimensionless mean velocity. At the needle wall, the electric potential is fixed and the liquid does not slip, i.e.,

$$\phi^i = \phi^e = 1, \quad u = w = 0. \tag{17}$$

We impose the standard regularity conditions

$$\phi_r^i = u = w_r = 0 \tag{18}$$

on the symmetry axis and the outflow conditions

$$u_z = w_z = F_z = (\sigma_e)_z = 0 \tag{19}$$

at the right-hand end $z_e = (H + L_n)/R_i$ of the computational domain (the red rectangle in Fig. 1).

For the configuration considered in this work, Gañán-Calvo et al. [23] found the following analytical solution for the far-field electric potential:

$$\phi_1(r', z') = \frac{-K_v}{\ln(4H'/R_i)} \ln \left\{ \frac{[r'^2 + (1 - z')^2]^{1/2} + (1 - z')}{[r'^2 + (1 + z')^2]^{1/2} + (1 + z')} \right\}, \tag{20}$$

where r' and z' are cylindrical coordinates with origin at the intersection between the symmetry axis and the grounded planar electrode (see Fig. 1) and K_v is a dimensionless constant that depends on the ratio H'/R_i. We take advantage of this solution to limit the calculations to the meniscus and the jet, leaving aside the charged spray. Specifically, we assume that the electric potential matches the analytical solution ϕ_1 at the boundary $r = r_e$ ($r_e \equiv R_e/R_i$). A logarithmic drop of voltage

$$\phi_2 = 1 - [1 - \phi_1(r_e, z_e')] \ln r / \ln r_e, \quad z_e' \equiv (H' + L_n)/R_i, \tag{21}$$

is applied at the boundary $z = 0$ and $1 < r < r_e$. Finally, the condition

$$\phi_z = (\phi_1)_z \tag{22}$$

is considered for the right-hand end $z = z_e$ of both the liquid and gas computational domains.

III. NUMERICAL PROCEDURES

We solved the problem formulated in the preceding section with two numerical schemes: a tracking interface technique proposed in this work and an adaptation of the volume-of-fluid (VOF) method developed by Popinet [18,19] and extended by López-Herrera et al. [20] to study EHD phenomena.

A. The proposed method

Since we search for steady solutions, we drop any time dependence in the Navier-Stokes equations (2)–(4). As mentioned in Sec. II, we assume that the characteristic electric time is much shorter than any hydrodynamic time and hence all the electrical charges are confined to the free surface ($\rho_e = 0$). In this case, the electric conductivity K can be regarded as constant. Because the liquid electrical permittivity is also assumed to be homogeneous, the electric forces vanish in the bulk domain and enter into the problem through the Maxwell stresses in the free surface boundary conditions.

A tracking interface technique was implemented to capture the steady liquid-gas interface position $r = F(z)$. We solved the nonlinear system of equations formed by the bulk equations (2)–(7), the interface equations (8)–(15), and the rest of the boundary conditions (16) and (17). In this way, one obtains the spatial dependence of the meniscus-jet shape F, the velocity and pressures fields (u, w, p) in the liquid domain, the surface charge density σ_e, and the inner and outer potential fields ϕ^i and ϕ^o. The current intensity I is the sum of the contributions due to the bulk conduction I_b and surface convection I_s, calculated at any axial position z along the cone jet as

$$I_b(z) = 2\pi \int_0^{F(z)} \alpha E_{iz}(r, z) r \, dr, \quad I_s(z) = 2\pi \sigma_e(z) v_s(z), \tag{23}$$

where v_s is the dimensionless liquid velocity at the interface. All these quantities are determined as functions of the five dimensionless control parameters C, v_e, β, χ, and α.

A boundary-fitted coordinate system [24] was used to calculate the solution. Both the liquid and the gas domains were mapped onto the fixed rectangular domain ($0 \leqslant \eta^{(l,g)} \leqslant 1, 0 \leqslant \xi \leqslant z_e$) by means of the coordinate transformations ($\eta^l = r/F, \xi = z$) and [$\eta^g = (r - F)/(r_e - F), \xi = z$] for the liquid and gas domains, respectively. The liquid and gas domains were discretized using n_{η^l} and n_{η^g} Chebychev spectral collocation points [25] along the η^l and η^g axes, respectively, while the axial direction ξ was discretized using n_ξ uniformly distributed points. We used fourth-order central finite differences to get the axial derivatives except close to the ξ boundaries, where second-order upwind finite differences were applied. All the simulations presented here were done with $n_{\eta^l} = 11$, $n_{\eta^g} = 20$, and $n_\xi = 160$.

The equations in the discretized domain yielded a system of $(4n_{\eta^l} + n_{\eta^g}) \times n_\xi + 2n_\xi$ nonlinear equations that was solved iteratively using a trust-region method [26] implemented in the MATLAB subroutine FSOLVE. The initial guess for the iterations was obtained as follows. For given values of C, β, χ, and α, we first set a sufficiently high liquid velocity v_e. Because a quasicylindrical jet is expected in this case, the equations were solved with $u = 0$, $w = 2v_e(1 - r^2)$, $F = 1$, and $\phi^i = \phi^e = 1$ as the initial guess. Once the algorithm converged to a solution, the control parameter space was explored using a continuation technique. The algorithm showed itself to be robust and computationally efficient. It converged to the sought solution for all the cases considered in less than 1 hour running on an Intel Xeon(R) X5670@2.93 GHz processor.

B. The VOF method

We also performed simulations using the open source fluid simulation engine GERRIS [27]. GERRIS is a VOF method originally conceived to deal with the time-dependent incompressible Euler equations [18]. It has since been improved and extended considerably to suit problems arising in such diverse fields as multiphase [19], geostrophic [28], granular [29], and EHD [20] flows. The VOF method treats immiscible fluids as a single one with spatially varying properties through the interface. Therefore, the balance equation (1) for the surface charge density cannot be explicitly considered. To circumvent this difficulty, the VOF method solves the evolution equation (A8) (see the Appendix) for the volumetric charge density ρ_e with $K =$ const. It simulates a transient regime that eventually reaches the steady cone-jet state of electrospray (provided that this state is stable for the selected values of the governing parameters). We have verified that the steady states reached in the simulations were consistent with the leaky-dielectric model, i.e., all the charges were confined in a very thin layer next to the interface. In this regard, one can assert that the numerical method converged to the steady solution of the leaky-dielectric model.

We set as initial condition a planar interface located inside the capillary tube. As time proceeds, the meniscus protrudes and a jet emerges by the action of electric forces. The simulation is continued until a stable meniscus jet is obtained. The grid is adapted at every time step according
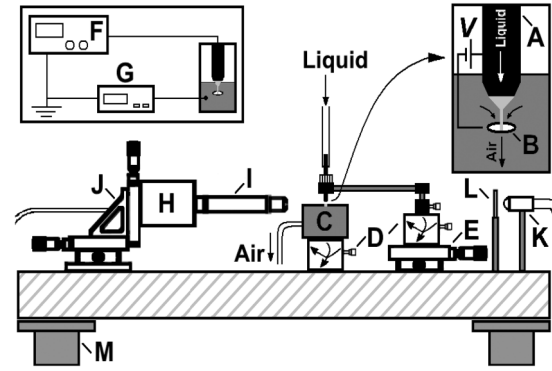

FIG. 2. Schematic diagram of the experimental setup.

to the charge distribution and the interface curvature. The minimum and maximum cell sizes at the last stage of the simulation were $h_{\min} = 3.91 \times 10^{-3}$ and $h_{\max} = 0.03125$, respectively. More details of the method are given elsewhere [20]. The algorithm converged to the sought solution in about 72 hours running on an Intel Xeon(R) X5670@2.93 GHz processor.

IV. EXPERIMENTAL METHOD

A. Experimental setup

The experimental setup is shown schematically in Fig. 2. The liquid was injected at a constant flow rate Q by a stepper motor through a capillary (A) of inner (outer) radius $R_i = 100$ ($R_o = 110$) μm located in front of a metallic plate at a distance $H' = 1$ mm. The plate had an orifice (B) 350 μm in diameter located in front of the capillary. The plate covered the upper face of a metallic cubic cell (C). We used a high-precision orientation system (D) and a translation stage (E) to ensure the correct alignment of these elements and to set the capillary-to-orifice distance H'. An electric potential V was applied to the end of the feeding capillary through a dc high voltage power supply (BERTAN 205B-10R) (F) and the cubic cell was used as ground electrode. A liquid meniscus was formed in the open air and stretched by the action of the electric field. A microjet tapered from the meniscus tip and moved vertically towards the plate orifice. A prescribed negative gauge pressure (about 10 mbars) was applied in the cubic cell by using a suction pump to produce an air stream coflowing with the jet. Both the liquid jet and the coaxial air stream crossed the plate orifice, which prevented liquid accumulation on the metallic plate. In this way, all the electric charges were collected in the cubic cell. Because the full scale of typical electric current measurements was in the nanoampere range, special care was taken for electrical shielding and grounding. The electric current I transported by the liquid jet was measured using a picoammeter (KEITHLEY model 6485) (G) connected to the cell. It must be noted that the mechanical effects associated with the gas stream were negligible (the air speed was smaller than about 10% of that of the liquid at the orifice and the density and pressure drops in the gas stream were smaller than about 2%). In addition, air ionization effects were less probable than in quiescent air because charges in the gas that could cause ionization cascades were flushed by the gas stream.
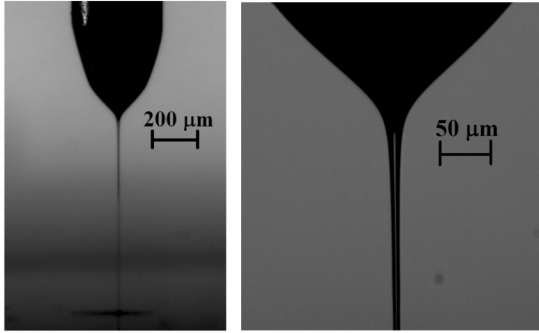
FIG. 3. The 1-octanol jet produced by the experimental setup described in the text. The left (right) image was acquired with the auxiliary (working) CCD camera.

Digital images of 1280×960 pixels were acquired using a CCD camera (AVT STRINGAY F-1125B) (H) equipped with optical lenses (an OPTEM HR $10\times$ magnification zoom objective and an OPTEM ZOOM 70XL set of lenses with variable magnification from $0.75\times$ to $5.25\times$) (I) providing a frame covering an area of about 443×332 μm^2. The magnification obtained was approximately 346 nm/pixel. The numerical aperture of the optical system was about 0.3. The camera could be displaced both horizontally and vertically using a triaxial translation stage (J) to focus the liquid meniscus. The fluid configuration was illuminated from the back by cool white light provided by an optical fiber (K) connected to a stroboscopic light source to reduce the image exposure time to about 3 μs. A frosted diffuser (L) was positioned between the optical fiber and the microjet to provide uniform lighting. To check that the fluid configuration was axisymmetric, we also acquired images of the liquid meniscus using an auxiliary CCD camera (not shown in Fig. 2) with an optical axis perpendicular to that of the main camera. All these elements were mounted on an optical table with a pneumatic antivibration isolation system (M) to damp the vibrations coming from the building.

Experiments were conducted with 1-octanol (PANREAC 99% ps) ($\rho = 827$ kg/m³, $\mu = 0.0081$ kg/ms, $\gamma = 0.0266$ N/m, $K = 9 \times 10^{-7}$ S/m, and $\beta = 10$). The surface tension was determined using the theoretical image fitting analysis method [30]. The electrical conductivity was measured by applying a voltage difference between the ends of a cylindrical borosilicate capillary full of the working liquid and then measuring the resulting electric current. The viscosity, density, and electrical permittivity were taken from the manufacturer's specifications. By way of illustration, Fig. 3 shows the image of a jet produced by the experimental setup described above with $Q = 0.5$ ml/h and $V = 1.6$ kV.

B. Image processing technique

We shall here briefly describe the main aspects of the image processing technique used to precisely determine the free surface position. Details of the procedure are given elsewhere [31,32]. The contours of the free surface in the image were detected using a two-stage procedure. In the first stage, a set of pixels probably corresponding to the contour being sought was extracted using Otsu's method [33]. The
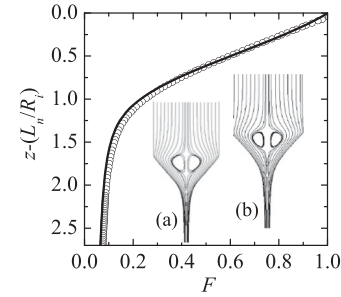

FIG. 4. Free surface position and streamlines calculated with the (a) tracking interface technique (solid line) and (b) VOF method (symbols) for $C = 0.18$, $\beta = 10$, $\alpha = 15.3$, $\chi = 10$, and $v_e = 0.02$.

accuracy of Otsu's method is limited to the pixel size. In the second stage, the accuracy of the detected contours was improved to the subpixel level by analyzing the gray intensity profile along the direction normal to the contour. Fitting the sigmoid (Boltzmann) function [34] to the gray intensity values allowed us to obtain a continuous function in the transient region of the gray profile. The contour point was found by applying the local thresholding criterion. The number of resulting contour points was approximately equal to the number of pixels of the image along the vertical direction. Once the left x_l and right x_r contours had been detected, they were rotated to their vertical position (the rotation angle was less than $2°$ in all the cases analyzed) and the symmetry axis was found. Small nonaxisymmetric perturbations of the free surface were ignored by considering the axisymmetric contour $F = (x_r - x_l)/2$. This quantity was compared with the numerical results.

V. RESULTS AND DISCUSSION

Numerical simulations of the problem formulated in Sec. II were conducted with the tracking interface technique proposed in this work (Sec. III A) and a VOF method [18,19] (Sec. III B). The following set of geometrical parameters was considered in all the simulations: $r_e = 6.67$, $L_n/R_i = 1.77$, $H/R_i = 9.4$, and $H'/R_i = 40$ (for which $K_v = 0.56$). In addition, the needle width was set to zero ($R_i = R_o$) in the proposed method, while the value $R_o/R_i = 1.22$ were selected in the VOF technique to improve the algorithm convergence.

Figure 4 shows a comparison between the two numerical methods for the set of parameters $C = 0.18$, $\beta = 10$, $\alpha = 15.3$, $\chi = 10$, and $v_e = 0.0182$, for which a stable meniscus-jet configuration was reached. The two methods predict almost the same free surface shape and show the existence of a recirculation cell inside the liquid meniscus. This recirculation pattern is caused by the action of the shear Maxwell stresses at the free surface, which drag along that surface an amount of liquid that cannot be exhausted by the thin emitted jet [16,35]. This flow structure is characteristic of low-viscosity liquids electrosprayed at small flow rates [36] and has also been observed in coflowing systems for the low Q range [37,38].

We also checked our tracking numerical method against experiment for two different cases. Figure 5 shows the results for the free surface position $F(z)$ of a 1-octanol meniscus jet produced by applying a voltage $V = 1600$ V while injecting
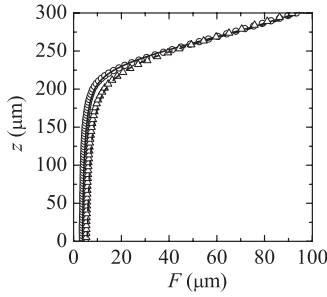
FIG. 5. Free surface position $F(z)$ of a 1-octanol meniscus jet produced with $V = 1600$ V and $Q = 0.5$ ml/h (circles and solid line) and $Q = 1$ ml/h (triangles and dashed line). The symbols and lines correspond to the experiments and proposed numerical method, respectively. Here F and z stand for the corresponding dimensional quantities and the z axis is the upward vertical axis with the origin at the bottom of the experimental image.

FIG. 7. Axial distribution of the total intensity (circles) and the contributions associated with the bulk conduction (triangles) and the surface convection (squares) calculated by the proposed method for the experimental case with $Q = 0.5$ ml/h. The shape of the meniscus jet (solid line) is also plotted to show where the transition between conduction and convection of charges takes place.

liquid at $Q = 0.5$ and 1 ml/h. These flow rates are close to the minimum value $Q_{min} \sim \gamma \varepsilon_0 (\rho K)^{-1} = 1.14$ ml/h for which the cone-jet mode is stable [3,7,39]. Indeed, we were not able to produce a stable 1-octanol jet for $Q < 0.5$ ml/h. The corresponding dimensionless parameters are $C = 0.182$, $\beta = 10$, $\alpha = 15.3$, $\chi = 10$, and $v_e = 0.00913$ and 0.0182 for $Q = 0.5$ and 1 ml/h, respectively. There is remarkable agreement between the experimental and numerical contours. The average deviation between them was less than 0.6 μm in both cases. The simulations captured perfectly the reduction of the jet radius when the flow rate was reduced by half. It is worth emphasizing that the agreement between the numerical and the experimental results for these limiting configurations shows the validity of the charge relaxation hypothesis [3,6,7,39] over the entire parameter space.

Optical diffraction renders the present fluid configuration almost opaque. Therefore, it is quite difficult to get information on the flow pattern inside the meniscus by standard experimental techniques such as microparticle image velocimetry or dye injection. In fact, Hayati *et al.* [35] had to use relatively large needles (1–2 mm in diameter) in their experimental visualizations. In contrast, numerical simulations allow not only the visualization of the recirculation cell taking place for small Q [16], but also the quantification of its size as Q decreases. Figure 6 illustrates this capability of the proposed numerical method.
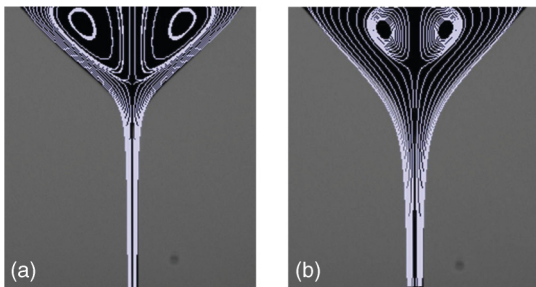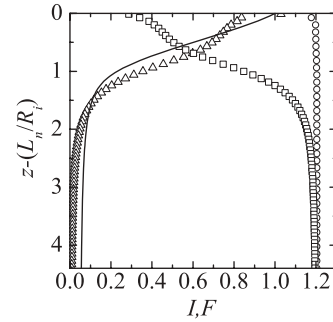

FIG. 6. (Color online) Streamlines plotted on the corresponding experimental images for a 1-octanol meniscus jet produced with $V = 1600$ V and (a) $Q = 0.5$ ml/h and (b) $Q = 1$ ml/h.

One of the most relevant quantities in electrospray is the electric current I transported by the jet. A proof of the consistency of our simulations is the global conservation of electric charge, which implies that the total electric current $I = I_b + I_s$ should remain constant along the meniscus jet. Figure 7 shows the axial distribution of the current intensities associated with the bulk conduction and the surface convection, as well as the total value, for the experimental case with $Q = 0.5$ ml/h. The values were made dimensionless with the characteristic intensity $I_0 = (\varepsilon_0 \gamma^2/\rho)^{1/2}$ [3,7]. As has been noted in theoretical works [3,7,11], bulk conduction is the dominant mechanism of charge transport in the meniscus, while surface convection is dominant in the jet region. The neck can be seen as the region where the transition between these two mechanisms takes place. The dimensionless intensity I/I_0 measured in the experiments was 1.4, reasonably close to the numerical prediction 1.2 and the scaling law $I/I_0 = 2.6(Q/Q_0)^{1/2} = 1.7$ [7].

To summarize, a robust and efficient simulation method has been proposed to simulate steady EHD phenomena. Calculations were greatly simplified in this method by assuming that the electric charges are accumulated within an infinitely thin layer at the interface and then electric forces result from the Maxwell stresses at that surface exclusively. The validity of the discretization scheme has been shown by comparing the results with those obtained with a much more sophisticated VOF method. The free surface position of the meniscus jet was measured very precisely in experiments with 1-octanol. The comparison between the numerical predictions for the liquid contour and the experimental results confirmed the validity of the proposed method. The numerical method also provided correct values of the emitted electric current even for configurations very close to the cone-jet stability limit.

APPENDIX: EQUATIONS OF THE VOF METHOD

In this Appendix we derive the equations solved by the VOF method from the Taylor-Melcher leaky-dielectric model [22]. The starting point is the Maxwell electrostatic equations

$$\nabla \cdot (\epsilon \mathbf{E}) = \rho_e, \tag{A1}$$

$$\nabla \times \mathbf{E} = 0, \tag{A2}$$

the Navier-Stokes equations

$$\nabla \cdot \mathbf{v} = 0, \tag{A3}$$

$$\rho \frac{D\mathbf{v}}{Dt} = -\nabla p - \frac{1}{2}\mathbf{E} \cdot \mathbf{E}\nabla\epsilon + \nabla \cdot (\epsilon\mathbf{E})\mathbf{E} + \mu\nabla^2\mathbf{v}, \tag{A4}$$

and the equations for the conservation of neutral and charged species

$$\frac{Dn^{(k)}}{Dt} = \nabla \cdot [-\omega^{(k)}ez^{(k)}n^{(k)}\mathbf{E} + \omega^{(k)}k_BT\nabla^2n^{(k)}] + r^{(k)}. \tag{A5}$$

Here $n^{(k)}$, $r^{(k)}$, $z^{(k)}$, and $\omega^{(k)}$ are the concentration, production rate by chemical reaction, valence, and mobility of the kth species, respectively, and k_B, e, and T are the Boltzmann constant, electron charge, and fluid temperature, respectively.

The charge density ρ_e can be calculated as

$$\rho_e = \sum_k ez^{(k)}n^{(k)}. \tag{A6}$$

A conservation equation for this variable can be readily derived by adding the equations (A5) for the different species:

$$\frac{D\rho_e}{Dt} = \nabla \cdot \left[-\left(\sum_k \omega^{(k)}e^2z^{(k)2}n^{(k)} \right)\mathbf{E} \right]$$
$$+ ek_BT \sum_k z^{(k)}\omega^{(k)}\nabla^2n^{(k)} + \sum_k ez^{(k)}r^{(k)}. \tag{A7}$$

In Eq. (A7), migration due to thermal diffusion (the second term of the right-side of the equation) can be neglected as compared to electromigration, provided that $\ell eE_0/k_BT \gg 1$ (ℓ and E_0 are the characteristic length and electric field, respectively). In electrospray, $\ell \sim (\gamma\varepsilon_o^2/\rho K^2)^{1/3}$ and $E_0 \sim$

$(\gamma/\varepsilon_0\ell)^{1/2}$ [3], which yields $\ell eE_0/k_BT \simeq 8 \times 10^3$ for 1-octanol. Therefore, thermal diffusion is negligible for the configurations considered in the present work.

The production rates $r^{(k)}$ depend on the concentrations of the species and the chemical kinetics of the reactions occurring in the system. Note that these reactions can be extremely complex and, on some occasions, unknown. In fact, the rates $r^{(k)}$ depend on each other because the production (destruction) of some species implies the destruction (production) of others. Therefore, care must be taken in the modeling of the chemical reactions to prevent overdetermination. Nevertheless, three scenarios are simple enough to be easily modeled. The first is the unipolar injection, where a single species generated at an upstream electrode migrates through the fluid with zero production rate. The second one is the evolution of strong electrolytes. In this case, neutral species are fully dissociated and chemical reactions are absent ($r^{(k)} = 0$). The last case is the evolution of a binary z-z electrolyte analyzed by Saville [22]. Three species are diluted in the fluid: the neutral, the ionic, and the counterionic. In the forward reaction, the neutral species dissociate, producing the same amount of ions and counterions, while in the recombination reaction the ionic and counterionic species disintegrate at the same rate to produce the neutral one. The source or sink term $\sum_k ez^{(k)}r^{(k)}$ in Eq. (A7) vanishes in the three cases described above. Taking into account these considerations, Eq. (A7) reduces to the expression

$$\frac{D\rho_e}{Dt} = \nabla \cdot (-K\mathbf{E}), \quad K = \sum_k \omega^{(k)}e^2z^{(k)2}n^{(k)}. \tag{A8}$$

In the leaky-dielectric model [22], all characteristic times of hydrodynamic nature in the bulk are much longer than the electrical relaxation time. Therefore, the volumetric charge density ρ_e is assumed to be zero and electrical charges are only allowed to exist at the interface. Therefore, Eq. (A8) reduces to

$$\nabla \cdot (K\mathbf{E}) = 0. \tag{A9}$$

It must be noted that [22] keeps the bulk electric forces in Eq. (A4), although, strictly speaking, they should be removed. Our VOF method solves Eqs. (A1)–(A4) and (A9) with $K =$ const.

---

[1] W. Gilbert, *De Magnete* (Short, London, 1600), Book 2, Chap. 2.

[2] A. Jaworek and A. Krupa, J. Aerosol Sci. **30**, 873 (1999).

[3] A. M. Gañán-Calvo, Phys. Rev. Lett. **79**, 217 (1997).

[4] J. F. de la Mora, Annu. Rev. Fluid Mech. **39**, 217 (2007).

[5] J. F. de la Mora and I. G. Loscertales, J. Fluid Mech. **260**, 155 (1994).

[6] A. M. Gañán-Calvo, J. Dávila, and A. Barrero, J. Aerosol Sci. **28**, 249 (1997).

[7] A. M. Gañán-Calvo, J. Aerosol Sci. **30**, 863 (1999).

[8] A. M. Gañán-Calvo and J. M. Montanero, Phys. Rev. E **79**, 066305 (2009).

[9] R. P. A. Hartman, D. J. Brunner, D. M. A. Camelot, J. C. M. Marijnissen, and B. Scarlett, J. Aerosol Sci. **30**, 823 (1999).

[10] F. Yan, B. Farouk, and F. Ko, J. Aerosol. Sci. **34**, 99 (2003).

[11] F. J. Higuera, J. Fluid Mech. **484**, 303 (2003).

[12] G. Taylor, Proc. R. Soc. London Ser. A **313**, 453 (1969).

[13] A. Barrero, A. Gañán-Calvo, J. Dávila, A. Palacio, and E. Gómez-González, J. Electrostat. **47**, 13 (1999).

[14] R. T. Collins, J. J. Jones, M. T. Harris, and O. A. Basaran, Nat. Phys. **4**, 149 (2008).

[15] S. N. Reznik, A. L. Yarin, E. Zussman, and L. Bercovici, Phys. Fluids **18**, 062101 (2006).

[16] O. Lastow and W. Balachandran, J. Electrostat. **64**, 850 (2006).

[17] L. K. Lim, J. Hua, C.-H. Wang, and K. A. Smith, AICHE J. **57**, 57 (2011).

[18] S. Popinet, J. Comput. Phys. **190**, 572 (2003).

[19] S. Popinet, J. Comput. Phys. **228**, 5838 (2009).

[20] J. M. López-Herrera, S. Popinet, and M. A. Herrada, J. Comput. Phys. **230**, 1939 (2011).

[21] J. M. López-Herrera, P. Riesco-Chueca, and A. M. Gañán-Calvo, Phys. Fluids **17**, 034106 (2005).

[22] D. A. Saville, Annu. Rev. Fluid Mech. **29**, 27 (1997).

[23] A. M. Gañán-Calvo, J. C. Lasheras, J. Dávila, and A. Barrero, J. Aerosol Sci. **25**, 22 (1994).

[24] J. F. Thompson, F. C. Thames, and C. M. Mastin, J. Comput. Phys. **47**, 1 (1982).

[25] M. R. Khorrami, Int. J. Numer. Methods Fluids **12**, 825 (1991).

[26] J. Nocedal and S. J. Wright, *Numerical Optimization*, edited by P. Glynn and S. M. Robinson, Springer Series in Operations Research (Springer, New York, 1999).

[27] S. Popinet, Gerris Flow Solver, http://gfs.sourceforge.net

[28] S. Popinet and G. Rickard, Ocean Model. **16**, 224 (2007).

[29] L. Staron, P.-Y. Lagree, and S. Popinet, J. Fluid Mech. **686**, 378 (2011).

[30] M. G. Cabezas, A. Bateni, J. M. Montanero, and A. W. Neumann, Colloids Surf. A **255**, 193 (2005).

[31] J. M. Montanero, C. Ferrera, and V. M. Shevtsova, Exp. Fluids **45**, 1087 (2008).

[32] E. J. Vega, J. M. Montanero, and C. Ferrera, Measurement **44**, 1300 (2011).

[33] N. Otsu, IEEE Trans. Syst. Man Cybernet. **9**, 62 (1979).

[34] B. Song and J. Springer, J. Colloid Interface Sci. **184**, 77 (1996).

[35] I. Hayati, A. I. Bailey, and T. F. Tadros, Nature (London) **319**, 41 (1986).

[36] A. Barrero, A. M. Gañán-Calvo, J. Dávila, A. Palacio, and E. Gómez-González, Phys. Rev. E **58**, 7309 (1998).

[37] S. L. Anna, N. Bontoux, and H. A. Stone, Appl. Phys. Lett. **82**, 364 (2003).

[38] M. A. Herrada, A. M. Gañán-Calvo, A. Ojeda-Monge, B. Bluth, and P. Riesco-Chueca, Phys. Rev. E **78**, 036323 (2008).

[39] A. M. Gañán-Calvo, J. Fluid Mech. **507**, 203 (2004).